Applied Physics Letters

Broadband spin-unlocked metasurfaces for bifunctional wavefront manipulations

Cite as: Appl. Phys. Lett. **120**, 181702 (2022); https://doi.org/10.1063/5.0091051
Submitted: 10 March 2022 • Accepted: 20 April 2022 • Published Online: 02 May 2022

Shaohua Dong, Shiqing Li, Xiaohui Ling, et al.

Applied Physics Letters ARTICLE scitation.org/journal/apl

Broadband spin-unlocked metasurfaces for bifunctional wavefront manipulations

Cite as: Appl. Phys. Lett. **120**, 181702 (2022); doi: 10.1063/5.0091051
Submitted: 10 March 2022 · Accepted: 20 April 2022 ·
Published Online: 2 May 2022

Shaohua Dong,[1,2] Shiqing Li,[2,3] Xiaohui Ling,[4,5] Guangwei Hu,[6] Yi Li,[1,7] Hongyi Zhu,[1,7,a)] Lei Zhou,[5] and Shulin Sun[2,8,a)]

AFFILIATIONS

[1]Peng Cheng Laboratory, Shenzhen 518055, China
[2]Shanghai Engineering Research Center of Ultra-Precision Optical Manufacturing, Department of Optical Science and Engineering, School of Information Science and Technology, Fudan University, Shanghai 200433, China
[3]College of Science, Zhejiang University of Technology, Hangzhou 310023, China
[4]College of Physics and Electronic Engineering, Hengyang Normal University, Hengyang 421002, China
[5]State Key Laboratory of Surface Physics, Key Laboratory of Micro and Nano Photonic Structures (Ministry of Education), and Department of Physics, Fudan University, Shanghai 200433, China
[6]Department of Electrical and Computer Engineering, National University of Singapore, Kent Ridge, Singapore 117583
[7]Shanghai Engineering Research Center for Broadband Technologies and Applications, Shanghai 200436, China
[8]Yiwu Research Institute of Fudan University, Zhejiang 322000, China

[a)]**Authors to whom correspondence should be addressed:** zhuhy@pcl.ac.cn and sls@fudan.edu.cn

ABSTRACT

Recently, Pancharatnam–Berry (PB) metasurfaces have exhibited powerful capabilities to control spin-polarized light. However, the adopted abrupt PB phase, introduced by simply rotating the basic elements, is spin-locked with opposite signs for different spin excitations, greatly limiting their practical applications. Here, we introduce a *high-efficiency* and *broadband* spin-unlocked metasurface with two mechanisms of a resonance phase and a geometric phase perfectly combined together. The design strategy is quite simple just through changing one geometric parameter rather than multi parameter optimization. As a proof of concept, the anomalous photonic spin Hall effect based on the spin-unlocked metasurface is demonstrated first, showing high experimental efficiency (over 80%) in a broad frequency range (11.3–16.6 GHz). Furthermore, another spin-unlocked metasurface is built to demonstrate the completely independent wavefront manipulations, i.e., the focusing effect and anomalous reflection. These findings significantly expand the electromagnetic control ability of a metasurface.

Electromagnetic metasurfaces, the two-dimensional (2D) equivalent of metamaterials, have been widely investigated as an ultrathin and compact platform for powerful manipulation of light.[1–7] Many fascinating effects and applications are extensively explored such as anomalous refraction/reflection,[8,9] flat metalens,[10–12] meta-holography,[13–16] surface wave excitation and control,[17–20] spin and orbital angular momentum manipulation,[21–24] unidirectional scattering,[25] asymmetric transportation,[26] anti-reflection,[27,28] and many others.[29–36] In general, the practical design of metasurfaces should rely on the local wave modulation enabled by varying the size (related to a resonance phase) and rotating angle (related to a geometric phase) of their individual artificial composite, i.e., meta-atoms.

As an example, anisotropic meta-atoms simply rotated by α can render a spin-dependent Pancharatnam–Berry (PB) geometric phase ($e^{-i\sigma 2\alpha}$).[14,37–44] Clearly, such responses of two opposite spin components [i.e., left circularly polarized (LCP, $\sigma = 1$) and right circularly polarized (RCP, $\sigma = -1$)] are essentially locked with the inverse phase profile, greatly limiting the information multiplexing [see Figs. 1(a) and 1(b)].[15,45,46] Recently, the resonance phase or propagation phase as a new degree of freedom can combine with the PB phase for a traditional PB metasurface to break the spin-correlated functional response [see Figs. 1(c) and 1(d)].[47] However, these designs either do not consider efficiency, which mainly attribute to the challenge to preserve the half-wave plate condition for all meta-atoms with their geometries continuously changed.[5,48–50] Meanwhile, most previous proposals are usually quite complex,[51–58] e.g., relying on the optimizations of multiple parameters.

In this work, we propose a simple metasurface design to realize high-efficiency spin-unlocked wavefront engineering within a broad

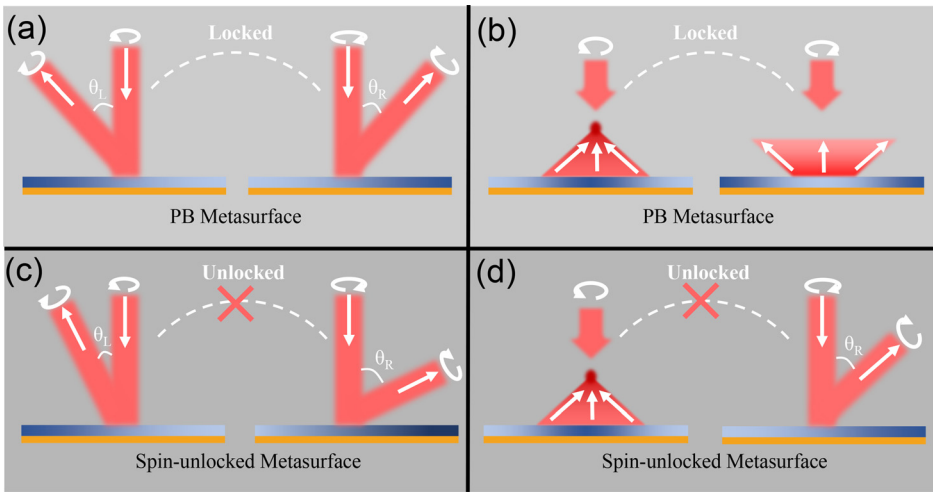

FIG. 1. Schematics of spin-locked wavefront modulations for traditional PB metasurfaces and the proposed spin-unlocked metasurfaces. (a) A traditional PB metasurface for realizing spin-dependent anomalous reflection along two mirror-symmetrical directions, i.e., photonic spin Hall effect (PSHE). (b) A traditional PB metasurface for realizing the spin-locked focusing and defocusing effect. (c) and (d) The proposed spin-unlocked metasurfaces for achieving completely independent bifunctional wavefront manipulations such as (c) mirror-asymmetric anomalous PSHE and (d) the focusing and anomalous reflection effects for two opposite spin waves.

frequency band. The building block cannot only provide a broadband resonance phase via simply tuning one geometric parameter but also always preserve its high polarization conversion ratio (PCR). As a proof of concept, an anomalous photonic spin Hall effect (APSHE) showing asymmetrical spin splitting is demonstrated based the spin-unlocked metasurface illuminated by a linear polarization (LP) wave. The experimentally measured efficiency can reach over 80% within 11.3–16.6 GHz. Furthermore, the more general spin-unlocked bifunctional EM manipulations are also realized such as the focusing effect for the LCP wave and anomalous reflection for the RCP wave. We firmly believe that, beyond the functions that are demonstrated in this work, more complicated high-performance dual-functionalities are easily realized following the proposed design principle. Our works provide a simple and powerful design scheme for spin photonics devices and expand the scope of metasurface-based polarization optics.

It is known that PB metasurfaces, composed of a series of meta-atoms with the identical structures but different orientations, can modulate the wavefronts of spin-polarized EM waves at will. While providing a phase distribution for the incident light with a certain CP (e.g., LCP), the metasurface will concomitantly achieve a contrary phase distribution for another CP (e.g., RCP) light, leading to the spin locked dual-functionalities as schematically shown in Figs. 1(a) and 1(b). To break such a correlation, we present the concept of the spin-unlocked metasurface via combining the freedoms of geometries and orientations into the designs of meta-atoms. As shown in Figs. 1(c) and 1(d), we can completely independently design the phase distributions for the incident light with different chirality. For example, the metasurface encoded with two different phase profiles can deflect the input LP beam to two asymmetrical non-specular reflection directions carrying different spins as shown in Fig. 1(c), giving rise to the APSHE. By carefully designing a spin-unlocked metasurface exhibiting a parabolic reflection-phase profile for LCP light and a linear-phase profile for RCP light, we can realize further two distinct functionalities as shown in Fig. 1(d).

We next introduce the basic concept to design a high-efficiency spin-unlocked metasurface. For an ideal PB metasurface, the composite meta-atom should possess specific anisotropic geometry behaving like a half-wave plate to completely flip the spin state of incident CP light.[21,39] The transmission/reflection phase distribution of such a metasurface can be generally described by $\phi(x,y) = \phi_{re} + \sigma\phi_{PB}(x,y)$. Here, $\phi_{PB}(x,y)$ is the PB phase profile determined by the meta-atoms' orientations $\alpha(x,y)$ [i.e., $\phi_{PB}(x,y) = 2\alpha(x,y)$], and $\sigma = \pm 1$ represents two different spin states of the input CP wave. Meanwhile, ϕ_{re} is a *spin-independent* basic phase shift originating from the EM resonances of the meta-atoms. Furthermore, if we introduce the inhomogeneous resonance phase distribution $\phi_{re}(x,y)$ via individually designing the dimensions of the local meta-atoms, two *distinct* phase profiles $\phi_L(x,y)$ and $\phi_R(x,y)$ can be encoded inside one metasurface for two different spin states

$$\begin{cases} \phi_{re}(x,y) + \phi_{PB}(x,y) = \phi_L(x,y), \\ \phi_{re}(x,y) - \phi_{PB}(x,y) = \phi_R(x,y). \end{cases} \tag{1}$$

As a result, two *independent* wavefront modulations can be offered by such a single metasurface. It should be noted that, although the spin-unlocked metasurfaces have been intensely explored, the *wideband* and *high-efficiency* performance still remains a challenge considering that all the meta-atoms of different dimensions should always satisfy the criterion of behaving like a half-wave plate in order to suppress the undesired normal mode.

We will introduce a dual-functional reflective metasurface with high efficiency and a broad frequency band. As a proof of concept, two linear phase profiles of different slopes are encoded inside the metasurface for LCP and RCP cases, creating the APHSE as schematically depicted in Fig. 1(c)

$$\begin{cases} \phi_L(x,y) + k_0 \sin(\theta_{iL})x = k_0 \sin(\theta_{rL})x, \\ \phi_R(x,y) + k_0 \sin(\theta_{iR})x = k_0 \sin(\theta_{rR})x, \end{cases} \tag{2}$$

where θ_{iL} and θ_{iR} (θ_{rL} and θ_{rR}) are the incident (reflective) angles for the impinging (outgoing) LCP and RCP beams, respectively, and k_0 is the total wavevector of an electromagnetic wave in free space. Next, we can further build up a spin-unlocked metasurface to realize more complex bifunctional wavefronts as schematically shown in Fig. 1(d), where $\phi_L(x,y)$ and $\phi_R(x,y)$, respectively, exhibit the parabolic and linear profiles

$$\begin{cases} \phi_L(x,y) = k_0\left(\sqrt{F^2+(x^2+y^2)} - F^2\right), \\ \phi_R(x,y) + k_0\sin(\theta_{iR})x = k_0\sin(\theta_{rR})x, \end{cases} \tag{3}$$

where F denotes the focal length. Obviously, we can substitute Eq. (2) or Eq. (3) into Eq. (1) to obtain both the $\phi_{re}(x,y)$ and $\phi_{PB}(x,y)$ for achieving the desired dual-functionalities, which can guide us to determine the geometric parameters of the metasurfaces, i.e., the geometric sizes and orientations of the meta-atoms at each local position.

We next introduce the practical designs of the desired meta-atoms that should not only provide desired resonance phase modulations but also meet the half-wave plate condition within a broad band. As shown in Fig. 2(b), the building block is a sandwich structure consisting of a metallic bending-H-shaped resonator and a ground metallic plane separated by a 3 mm-thick dielectric spacer ($\varepsilon_r = 3 + 0.01i$). We can flexibly modulate the resonance phase just by varying the opening angle θ of the meta-atom. Figures 2(c) and 2(d) depict finite-difference time domain (FDTD)-simulated PCR (described by $|r_{LL}|^2$) and spin-independent resonance phase ϕ_{re} [described as $\arg(r_{LL})$] as functions of the opening angle and frequency. It should be noted that the spin state of an anomalous reflection beam is eventually conserved considering that the direction of an outgoing beam is reversed in such a reflection-type system. We can see that PCR of the meta-atom can approach 100% within a broad frequency band of 10–18 GHz [see Fig. 2(c)], implying that these meta-atoms of different dimensions can always preserve the half-wave plate condition. The underlying mechanism of our meta-atom is explained as follows. Illuminated by impinging waves, the electric currents are induced inside the top bending-H structure and the bottom ground plane, giving rise to the magnetic resonance. While the opening angle of the H structure is varied, the resonance frequencies for two orthogonal LPs can be tuned simultaneously. Via carefully optimizing the Q factor and structural anisotropy, the half wave plate condition can be well maintained in a broad band. Moreover, the ϕ_{re} can cover a large modulation range within the broad band. Therefore, we can utilize the relation of $\phi_{re} \sim \theta$ to obtain a series of meta-atoms to construct the desired dual-functional metasurface. In addition, the PB phase profile only depends on the orientations of local meta-atoms, i.e., $\phi_{PB}(x,y) = 2\alpha(x,y)$. Finally, the desired spin-unlocked metasurface achieving two completely *independent* wavefronts can be obtained based on the database presented in Fig. 2.

As a proof of concept, a spin-unlocked metasurface working at the microwave regime for achieving APSHE has been experimentally demonstrated. Here, the anomalous reflection angles of the spin-unlocked metasurface are designed as $\theta_{rL} = -30°$ and $\theta_{rR} = 50°$, respectively, for two opposite spin waves at 12 GHz. Figure 3(a) shows the experimental setup to measure the scattered far-field distribution of the fabricated metasurface. Obviously, both the geometric sizes and orientations of the meta-atoms are varied along the x direction. FDTD simulated reflection phase distributions of the spin-unlocked metasurface for two opposite spin states at 12 GHz are shown in Fig. 3(b), according to the theoretical designs of Eq. (2). Here, a source horn is placed above the metasurface to shine a normally incident CP plane wave on the metasurface, and another CP receiver horn is rotated to measure the scattered electric field intensities of the specific spin state. Two CP horn antennas are connected to a vector network analyzer (Agilent E8362CPNA). Figures 3(c) and 3(d) depict the angular distributions of scattered electric field intensities at three representative frequencies of 10, 12, and 16 GHz for the spin-unlocked metasurface. As the metasurface is illuminated by the LCR or RCP beam, the opposite spin waves are steered to asymmetrical directions, exhibiting the so-called APSHE as depicted in Fig. 1(c). Obviously, experimental measurements match well with FDTD simulations.

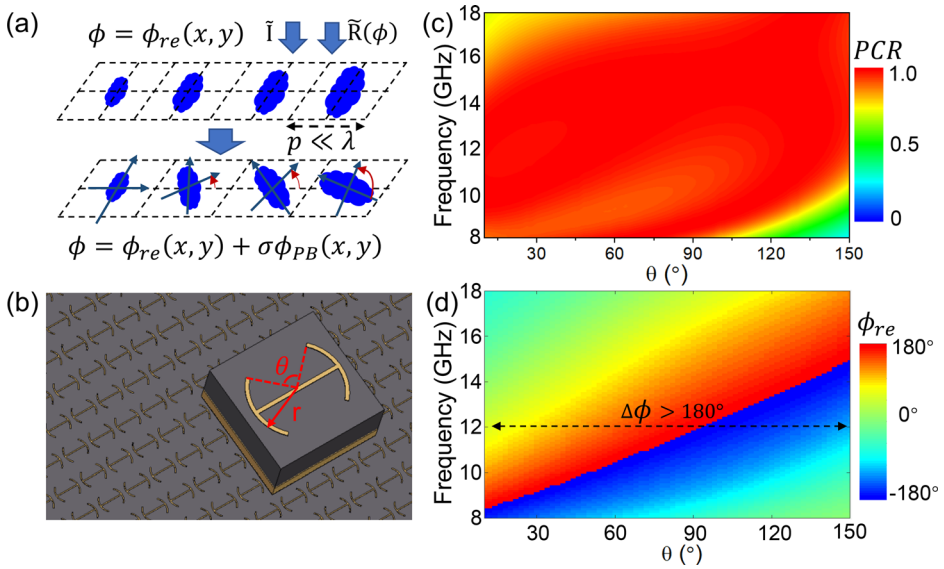

FIG. 2. Physical concept and practical design of the spin-unlocked metasurfaces. (a) Schematic of the spin-unlocked metasurface built by combining both the resonance phase $\phi_{re}(x,y)$ (depending on the size of the microstructure) and the PB phase (depending on the orientation of the microstructure) with the total phase response described by $\phi(x,y) = \phi_{re}(x,y) + \sigma\phi_{PB}(x,y)$. (b) Picture of the meta-atom (sized 6×6 mm^2) array composed of a metallic bending-H-shaped resonator (with $r = 2.5$ mm) and a metallic mirror separated by a 3 mm-thick dielectric layer. Here, the opening angle θ is a tunable parameter to modulate the resonance phase. (c) and (d) FDTD simulated *PCR* (c) and resonance phase ϕ_{re} (d) for the meta-atoms as functions of opening angle θ and frequency.

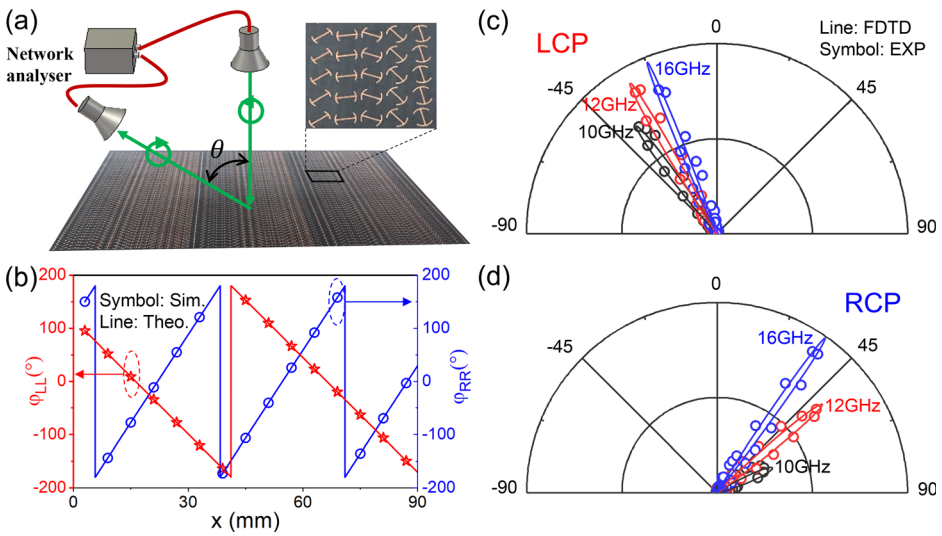

FIG. 3. Characterization of the anomalous photonic spin Hall effect by the proposed spin-unlocked metasurface. (a) Schematic of the scattered far-field measurement setup in our experiments. The inset depicts the picture of the part of the fabricated sample with both the sizes and orientations of the meta-atoms varied along the x direction. (b) The reflection phase distributions along the x direction of the spin-unlocked metasurface illuminated by the LCP and RCP beam at the designed frequency 12 GHz. (c) and (d) Measured and simulated normalized angular far-field distributions of the spin-unlocked metasurface for LCP (c) and RCP (d) light incidence at several frequencies.

The spin-unlocked metasurface can achieve high-performance APSHE within a broadband frequency. Figures 4(a) and 4(e) [Figs. 4(c) and 4(g)] show the FDTD-simulated (experimentally measured) co-polarized and cross-polarized angular distributions of scattered electric far-field intensities for LCP ($|+\rangle$) incidence. Similarly, Figs. 4(b) and 4(f) [Figs. 4(d) and 4(h)] show the FDTD-simulated (experimentally measured) co-polarized and cross-polarized angular distributions of scattered electric far-field intensities for RCP ($|-\rangle$) beam

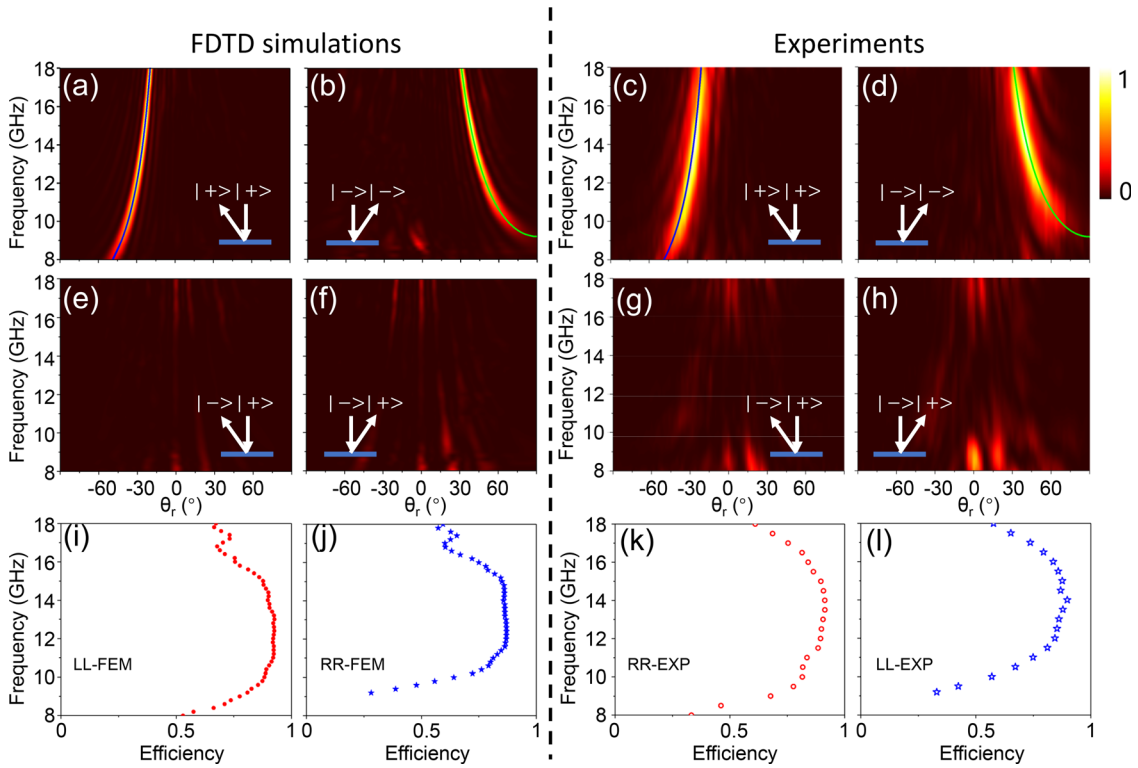

FIG. 4. Verification of high-efficiency and broadband APSHE. Simulated (a), (b), (e), and (f) and measured (c), (d), (g), and (h) normalized scattered-field intensities (color map) vs frequency and detecting angle for the spin-unlocked metasurface illuminated by normally incident LCP (a) and (e) and (c) and (g) and RCP (b) and (f) and (d) and (h) beams with receivers chosen as a LCP (a) and (f) and (c) and (h) and RCP (b) and (e) and (d) and (g) antennas, respectively. Here, solid lines in (a)–(d) are calculated in Eq. (2) under the normal-incidence condition. (c) and (f) APSHE efficiencies retrieved by simulation (i) and (j) and experiment (k) and (l) data vs frequency for LCP (i) and (k) and RCP (j) and (l) incidences.

incidence. Both of FDTD simulations and microwave experiments demonstrate that the asymmetrically anomalous reflections indeed exist within a quite broad frequency (8–18 GHz) for LCP and RCP incidences, agreeing well with the theoretical prediction (solid line) of Eq. (2). In Fig. 4(b) or Fig. 4(d), since the phase gradient $d\phi_R/dx$ is larger than k_0 below the frequency 9.2 GHz, the anomalous reflection beam will disappear in the far-field. As shown in Figs. 4(e)–4(h), the normal reflection modes carrying the opposite spin state are extremely small, implying the high performance of the meta-device. Figures 4(i) and 4(j) [Figs. 4(k) and 4(l)] exhibit the retrieved efficiencies of APSHE from simulations (experiments) at different frequencies, which are defined by the ratio between the integrated power of the anomalous reflection beam and that of the impinging beam. Our experimental results indicate that the spin-unlocked metasurface possesses high efficiencies of over 80% within about 11.3–16.6 GHz. Owing to the distinct deflection angles, the spin-decoupled metasurface shows different efficiencies for LCP and RCP cases [see Figs. 4(i)–4(l)]. Such a difference becomes significant for the large beam deflection region, where the local field approximation will be not valid anymore.[59,60]

Except for APSHE, more complex spin-unlocked bifunctional wavefront modulations have been further demonstrated. Based on the same database of meta-atoms presented above, we design a bifunctional metasurface to realize the focusing effect for LCP and anomalous reflection for RCP, as schematically shown in Fig. 1(d). Figure 5(a) illustrates the experimental setup of near-field mapping measurement to clarify the first functionality of our metadevice, i.e., the 3D focusing effect. In these experiments, we shine an LCP beam normally on the measurface by a horn antenna and adopt a monopole antenna to scan the electric field distributions in xoz and yoz. Both the monopole antenna and the horn antenna are connected to the vector network analyzer. Figure 5(b) shows part of the fabricated sample ($198 \times 198\ mm^2$) and the desired phase distribution $\phi_L(x, y)$ for realizing the 3D focusing effect with a focal length of 100 mm at 12 GHz. The simulated scattered $|E_x|^2$ field distribution in both xoz and yoz planes at 12 GHz is depicted in Fig. 5(c), obtained through subtracting the incident field from the total field, clearly verifying the 3D focusing effect with the focal length in good agreement with theoretical prediction. In our experiments, the monopole antenna is used to scan the area of $180 \times 180\ mm^2$ with the center located at 100 mm above the metasurface. Figure 5(d) shows the measured E_x field pattern in the xoz plane at seven representative frequencies within the broad frequency band of 9–15 GHz, which match well with the corresponding FDTD simulations depicted in Fig. 5(e). Clearly, such a robust focusing effect demonstrates the broadband characteristics of our device. However, the reflection phases do not always keep parabolic shape well outside the working band, leading to the deteriorated focusing quality.

Figure 6 exhibits the second functionality, i.e., anomalous reflection, of the spin-unlocked metasurface under the illumination of the RCP beam. According to the theoretical design, the reflection phase distribution at 12 GHz, including both the resonance phase and PB phase described in Eq. (3), satisfies a linear distribution along the x direction [see the bottom part of Fig. 6(a)], corresponding to the anomalous reflection angle of 45° at 12 GHz. Similar to previous

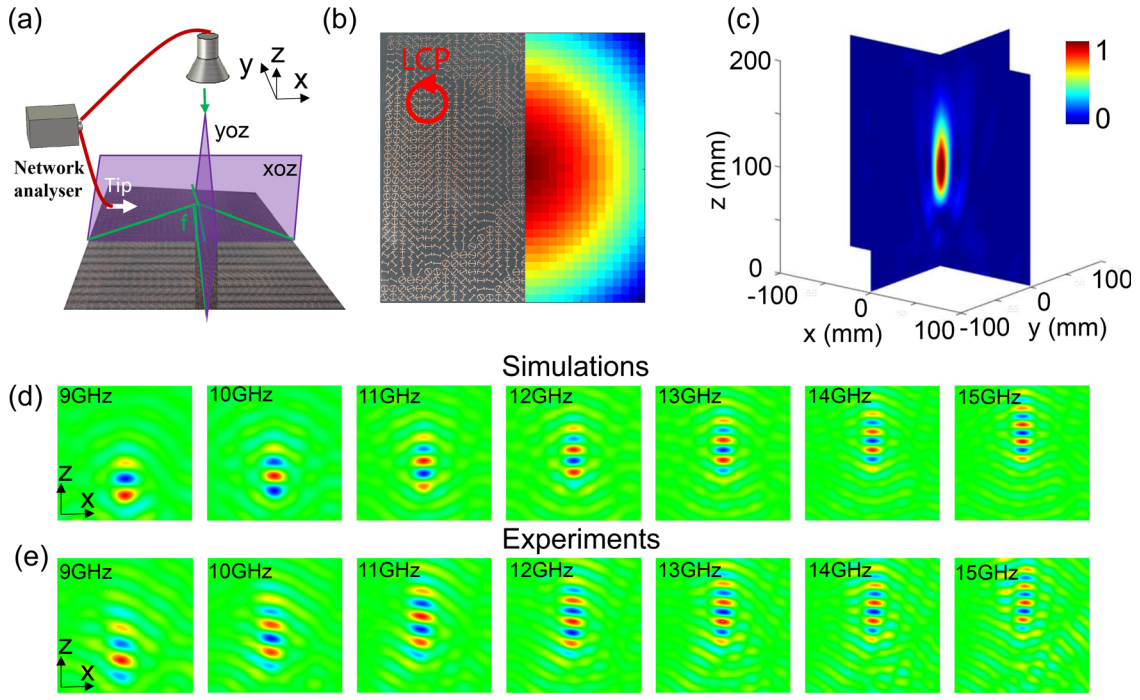

FIG. 5. Characterization of the focusing effect with the proposed spin-unlocked metasurface for the LCP beam. (a) Schematic of our experimental setup of the scattering near-field scanning measurement. (b) Part of the fabricated spin-unlocked metasurface and the reflection phase distribution of meta-atoms for normal incidence of the LCP beam at the designed frequency 12 GHz. (c) Simulated 3D reflected electric field intensity distribution of our device at 12 GHz. Here, the focal length is demonstrated as 100 mm. Reflected field patterns in the xoz plane obtained via simulations (d) and measurements (e) at several frequencies.

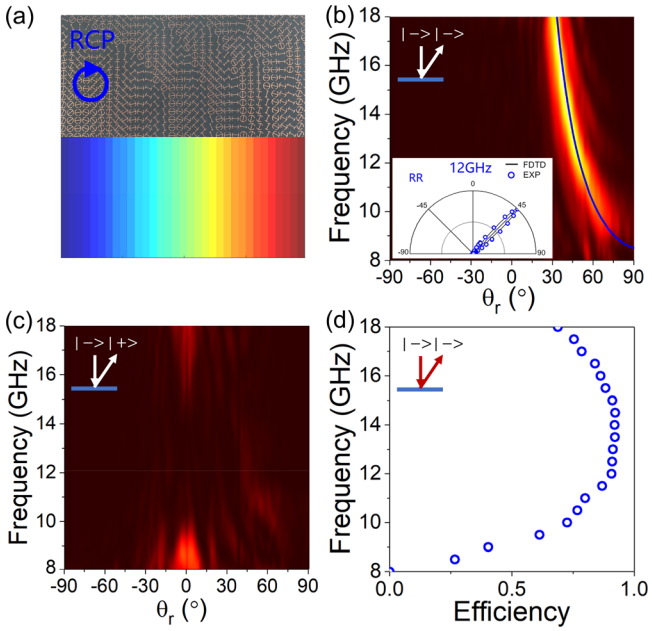

FIG. 6. Characterization of the anomalous reflection with the proposed spin-unlocked metasurface for the RCP beam. (a) The reflection phase distribution at 12 GHz. Measured normalized scattered-field intensities (color map) vs frequency and detecting angle for the spin-unlocked metasurface normally illuminated by the RCP beam, received by RCP (b) and LCP (c) horn antennas. The inset in (b) depicts the simulated and measured angular far-field intensity distributions at the designed frequency 12 GHz. (d) The anomalous reflection efficiencies vs frequency for the spin-unlocked metasurface retrieved by the experimental data in (b) and (c).

far-field measurements, we, respectively, use the LCP and RCP horn antenna to receive the scattered far-field signal of the metasurface at different reflection angles. The measured co-polarized and cross-polarized angular distributions of scattered electric far-field intensities (color map) vs frequency and reflection angle are shown in Figs. 6(b) and 6(c), respectively. Obviously, the scattered field power is mainly deflected to a specific angle, satisfying the expected value calculated in Eq. (3) [see the solid line in Fig. 6(b)]. The inset in Fig. 6(b) depicts the FDTD-simulated and experimentally measured scattered far-field distributions at 12 GHz as example, showing good agreement with each other. Based on the data from Figs. 6(b) and 6(c), we have also retrieved the measured efficiencies of the anomalous reflection effect for the spin-unlocked metasurface, remaining above 80% within 11–16.5 GHz. With these meta-atoms at hand, we can achieve arbitrary spin-modulated bifunctional wavefronts with quite high efficiency within the broad frequency band.

To summarize, a high-performance and broadband spin-unlocked bifunctional metasurface working at microwave frequencies is designed and demonstrated through combining the resonance phase and PB geometric phase together. Compared to the literature,[20,51–57] the proposed building block can provide the desired resonance phase with the PCR always remained at almost 100% within a broad band via single parameter tuning. The spin-delinked bifunctional wavefront modulations, i.e., APSHE and focus effect/anomalous reflection, are demonstrated by both simulations and experiments, exhibiting quite high efficiencies within a wideband. This design strategy is quite general that can be developed to THz and optical frequency regimes, where the nano-fabrication and Ohmic absorption will become the key challenges. Our findings pave up a promising direction to explore the spin-modulated multifunctional meta-system for high-integration and high-performance photonics applications.

This work was supported by the National Key R&D Program of China (Nos. 2020YFA0710100, 2020YFB1806405, and 2017YFA0700202), the Major Key Project of PCL (No. PCL2021A04), the National Natural Science Foundation of China (Nos. 12004258 and 11874118), and the Shanghai Science and Technology Innovation Action Plan (No. 20511102102).

AUTHOR DECLARATIONS

Conflict of Interest

The authors have no conflicts to disclose.

Author Contributions

S.D. and S.L. contributed equally to this work.

DATA AVAILABILITY

The data that support the findings of this study are available from the corresponding authors upon reasonable request.

REFERENCES

[1]S. Sun, Q. He, J. Hao, S. Xiao, and L. Zhou, "Electromagnetic metasurfaces: Physics and applications," Adv. Opt. Photonics **11**, 380–479 (2019).
[2]N. Yu and F. Capasso, "Flat optics with designer metasurfaces," Nat. Mater. **13**, 139–150 (2014).
[3]G. Cao, H. X. Xu, L. M. Zhou *et al.*, "Infrared metasurface-enabled compact polarization nanodevices," Mater. Today **50**, 499–515 (2021).
[4]H. H. Hsiao, C. H. Chu, and D. P. Tsai, "Fundamentals and applications of metasurfaces," Small Methods **1**, 1600064 (2017).
[5]A. Arbabi, Y. Horie, M. Bagheri, and A. Faraon, "Dielectric metasurfaces for complete control of phase and polarization with subwavelength spatial resolution and high transmission," Nat. Nanotechnol. **10**, 937–943 (2015).
[6]H. X. Xu, G. Hu, L. Han *et al.*, "Chirality-assisted high-efficiency metasurfaces with independent control of phase, amplitude, and polarization," Adv. Opt. Mater. **7**, 1801479 (2019).
[7]G. Hu, M. Wang, Y. Mazor, C. W. Qiu, and A. Alù, "Tailoring light with layered and moiré metasurfaces," Trends Chem. **3**, 342–358 (2021).
[8]N. Yu, P. Genevet, M. A. Kats, F. Aieta, J. P. Tetienne, F. Capasso, and Z. Gaburro, "Light propagation with phase discontinuities: Generalized laws of reflection and refraction," Science **334**, 333–337 (2011).
[9]S. Sun, Q. He, S. Xiao *et al.*, "Gradient-index meta-surfaces as a bridge linking propagating waves and surface waves," Nat. Mater. **11**, 426 (2012).
[10]A. Arbabi, Y. Horie, A. J. Ball, M. Bagheri, and A. Faraon, "Subwavelength-thick lenses with high numerical apertures and large efficiency based on high-contrast transmitarrays," Nat. Commun. **6**, 7069 (2015).
[11]M. Khorasaninejad, W. T. Chen, R. C. Devlin, J. Oh, A. Y. Zhu, and F. Capasso, "Metalenses at visible wavelengths: Diffraction-limited focusing and subwavelength resolution imaging," Science **352**, 1190 (2016).
[12]C. Hao, S. Gao, Q. Ruan, Y. Feng, Y. Li, J. K. Yang, Z. Li, and C. W. Qiu, "Single-layer aberration-compensated flat lens for robust wide-angle imaging," Laser Photonics Rev. **14**, 2000017 (2020).
[13]L. Huang, X. Chen, H. Mühlenbernd *et al.*, "Three-dimensional optical holography using a plasmonic metasurface," Nat. Commun. **4**, 2808 (2013).
[14]G. Zheng, H. Mühlenbernd, M. Kenney, G. Li, T. Zentgraf, and S. Zhang, "Metasurface holograms reaching 80% efficiency," Nat. Nanotechnol. **10**, 308 (2015).

[15]W. T. Chen, K. Y. Yang, C. M. Wang *et al.*, "High-efficiency broadband meta-hologram with polarization-controlled dual images," Nano Lett. **14**, 225 (2014).
[16]L. Jin, Y. W. Huang, Z. Jin *et al.*, "Dielectric multi-momentum meta-transformer in the visible," Nat. Commun. **10**, 4789 (2019).
[17]S. Dong, Y. Zhang, H. Guo, J. Duan, F. Guan, Q. He, H. Zhao, L. Zhou, and S. Sun, "Highly efficient wave-front reshaping of surface waves with dielectric metawalls," Phys. Rev. Appl. **9**, 014032 (2018).
[18]S. Dong, Z. Wang, H. Guo, F. Guan, X. Li, Q. He, H. Zhao, L. Zhou, and S. Sun, "Dielectric meta-walls for surface plasmon focusing and Bessel beam generation," Europhys. Lett. **122**, 67002 (2018).
[19]S. Dong, Q. Zhang, G. Cao *et al.*, "On-chip trans-dimensional plasmonic router," Nanophotonics **9**, 3357 (2020).
[20]S. Li, Z. Wang, S. Dong *et al.*, "Helicity-delinked manipulations on surface waves and propagating waves by metasurfaces," Nanophotonics **9**, 3473–3481 (2020).
[21]W. Luo, S. Xiao, Q. He, S. Sun, and L. Zhou, "Photonic spin hall effect with nearly 100% efficiency," Adv. Opt. Mater. **3**, 1102–1108 (2015).
[22]J. Ni, S. Liu, G. Hu, Y. Hu, Z. Lao, J. Li, Q. Zhang, D. Wu, S. Dong, J. Chu, and C. W. Qiu, "Giant helical dichroism of single chiral nanostructures with photonic orbital angular momentum," ACS Nano **15**, 2893–2900 (2021).
[23]X. Ling, F. Guan, X. Cai, S. Ma, H. Xu, Q. He, S. Xiao, and L. Zhou, "Topology-induced phase transitions in spin-orbit photonics," Laser Photonics Rev. **15**, 2000492 (2021).
[24]F. Guan, Y. Hu, X. Dai, X. Ling, S. Ma, J. Lin, S. Dong, and Y. Xiang, "Spin-orbit interactions in a nonlinear medium due to a nonlinear-induced geometric phase," Opt. Lett. **46**, 2758–2761 (2021).
[25]S. Dong, G. Hu, Q. Wang *et al.*, "Loss-assisted metasurface at an exceptional point," ACS Photonics **7**, 3321–3327 (2020).
[26]H. Chu, X. Xiong, Y. Gao, J. Luo, H. Jing, C. Li, R. Peng, M. Wang, and Y. Lai, "Diffuse reflection and reciprocity-protected transmission via a random-flip metasurface," Sci. Adv. **7**, eabj0935 (2021).
[27]H. Chu, H. Zhang, Y. Zhang, R. Peng, M. Wang, Y. Hao, and Y. Lai, "Invisible surfaces enabled by the coalescence of anti-reflection and wavefront controllability in ultrathin metasurfaces," Nat. Commun. **12**, 4523 (2021).
[28]G. Lavigne and C. Caloz, "Generalized Brewster effect using bianisotropic metasurfaces," Opt. Express **29**, 11361 (2021).
[29]J. Hao, Y. Yuan, L. Ran, T. Jiang, J. A. Kong, C. T. Chan, and L. Zhou, "Manipulating electromagnetic wave polarizations by anisotropic metamaterials," Phys. Rev. Lett. **99**, 063908 (2007).
[30]T. J. Cui, M. Q. Qi, X. Wan, J. Zhao, and Q. Cheng, "Coding metamaterials, digital metamaterials and programmable metamaterials," Light: Sci. Appl. **3**, e218 (2014).
[31]C. Pfeiffer, C. Zhang, V. Ray, L. J. Guo, and A. Grbic, "High performance bianisotropic metasurfaces: Asymmetric transmission of light," Phys. Rev. Lett. **113**, 023902 (2014).
[32]Y. Bao, Y. Yu, H. Xu *et al.*, "Coherent pixel design of metasurfaces for multidimensional optical control of multiple printing-image switching and encoding," Adv. Funct. Mater. **28**, 1805306 (2018).
[33]G. Hu, X. Hong, K. Wang *et al.*, "Coherent steering of nonlinear chiral valley photons with a synthetic Au-WS_2 metasurface," Nat. Photonics **13**, 467 (2019).
[34]K. Chen, G. Ding, G. Hu *et al.*, "Directional Janus metasurface," Adv. Mater. **32**, 1906352 (2020).
[35]D. Lee, S. So, G. Hu, M. Kim, T. Badloe, H. Cho, J. Kim, H. Kim, C.-W. Qiu, and J. Rho, "Hyperbolic metamaterials: Fusing artificial structures to natural 2D materials," eLight **2**, 1 (2022).
[36]X. Wang, A. Díaz-Rubio, and S. A. Tretyakov, "Independent control of multiple channels in metasurface devices," Phys. Rev. Appl. **14**, 024089 (2020).
[37]S. Pancharatnam, "Generalized theory of interference, and its applications," Resonance **18**, 387–389 (2013).
[38]M. V. Berry, "The adiabatic phase and Pancharatnam's phase for polarized light," J. Mod. Opt. **34**, 1401–1407 (1987).
[39]W. Luo, S. Sun, H. X. Xu, Q. He, and L. Zhou, "Transmissive ultrathin Pancharatnam-Berry metasurfaces with nearly 100% efficiency," Phys. Rev. Appl. **7**, 044033 (2017).
[40]X. Chen, L. Huang, H. Mühlenbernd *et al.*, "Dual-polarity plasmonic metalens for visible light," Nat. Commun. **3**, 1198 (2012).
[41]L. Zhang, S. Liu, L. Li, and T. J. Cui, "Spin-controlled multiple pencil beams and vortex beams with different polarizations generated by Pancharatnam-Berry coding metasurfaces," ACS Appl. Mater. Interfaces **9**, 36447–36455 (2017).
[42]X. Ding, F. Monticone, K. Zhang *et al.*, "Ultrathin Pancharatnam-Berry metasurface with maximal cross-polarization efficiency," Adv. Mater. **27**, 1195–1200 (2015).
[43]H. Xu, H. Liu, X. Ling, Y. Sun, and F. Yuan, "Broadband vortex beam generation using multimode Pancharatnam-Berry metasurface," IEEE Trans. Antennas Propagat. **65**, 7378–7382 (2017).
[44]D. Wen, F. Yue, G. Li *et al.*, "Helicity multiplexed broadband metasurface holograms," Nat. Commun. **6**, 8241 (2015).
[45]L. Zhang, R. Wu, G. Bai *et al.*, "Transmission-reflection-integrated multifunctional coding metasurface for full-space controls of electromagnetic waves," Adv. Funct. Mater. **28**, 1802205 (2018).
[46]T. Cai, S. Tang, G. Wang, H. Xu, S. Sun, Q. He, and L. Zhou, "High-performance bifunctional metasurfaces in transmission and reflection geometries," Adv. Opt. Mater. **5**, 1600506 (2017).
[47]Y. Qiu, S. Tang, T. Cai, H. Xu, and F. Ding, "Fundamentals and applications of spin-decoupled Pancharatnam-Berry metasurfaces," Front. Optoelectron. **14**, 134–147 (2021).
[48]J. P. B. Mueller, N. A. Rubin, R. C. Devlin, B. Groever, and F. Capasso, "Metasurface polarization optics: Independent phase control of arbitrary orthogonal states of polarization," Phys. Rev. Lett. **118**, 113901 (2017).
[49]R. C. Devlin, A. Ambrosio, N. A. Rubin, J. P. B. Mueller, and F. Capasso, "Arbitrary spin-to-orbital angular momentum conversion of light," Science **358**, 896–901 (2017).
[50]R. Jin, L. Tang, J. Li, J. Wang, Q. Wang, Y. Liu, and Z. Dong, "Experimental demonstration of multidimensional and multifunctional metalenses based on photonic spin Hall effect," ACS Photonics **7**, 512–518 (2020).
[51]B. Groever, N. A. Rubin, J. P. Mueller, R. C. Devlin, and F. Capasso, "High-efficiency chiral meta-lens," Sci. Rep. **8**, 7240 (2018).
[52]H. Xu, L. Han, Y. Li, Y. Sun, J. Zhao, S. Zhang, and C. W. Qiu, "Completely spin-decoupled dual-phase hybrid metasurfaces for arbitrary wavefront control," ACS Photonics **6**, 211–220 (2019).
[53]H. Xu, G. Hu, Y. Li *et al.*, "Interference-assisted kaleidoscopic meta-plexer for arbitrary spin-wavefront manipulation," Light: Sci. Appl. **8**, 3 (2019).
[54]Z. Wang, J. Wu, L. Wu, Y. Gou, H. Ma, Q. Cheng, and T. Cui, "High efficiency polarization-encoded holograms with ultrathin bilayer spin-decoupled information metasurfaces," Adv. Opt. Mater. **9**, 2001609 (2021).
[55]R. Ji, X. Xie, X. Guo, Y. Zhao, C. Jin, K. Song, S. Wang, J. Yin, Y. Liu, C. Jiang, and C. Yang, "Chirality-assisted Aharonov-Anandan geometric-phase metasurfaces for spin-decoupled phase modulation," ACS Photonics. **8**, 1847–1855 (2021).
[56]W. Guo, G. Wang, X. Luo, H. Hou, K. Chen, and Y. Feng, "Ultrawideband spin-decoupled coding metasurface for independent dual-channel wavefront tailoring," Ann. Phys. **532**, 1900472 (2020).
[57]D. Wang, T. Liu, Y. Zhou, X. Zheng, S. Sun, Q. He, and L. Zhou, "High-efficiency metadevices for bifunctional generations of vectorial optical fields," Nanophotonics **10**, 685–695 (2020).
[58]Y. Yuan, K. Zhang, B. Ratni, Q. Song, X. Ding, Q. Wu, S. N. Burokur, and P. Genevet, "Independent phase modulation for quadruplex polarization channels enabled by chirality-assisted geometric-phase metasurfaces," Nat. Commun. **11**, 4186 (2020).
[59]N. M. Estakhri and A. Alu, "Wave-front transformation with gradient metasurfaces," Phys. Rev. X **6**, 041008 (2016).
[60]A. Díaz-Rubio, V. S. Asadchy, A. Elsakka, and S. A. Tretyakov, "From the generalized reflection law to the realization of perfect anomalous reflectors," Sci. Adv. **3**, e1602714 (2017).